RSC Advances

PAPER

View Article Online
View Journal | View Issue

Cite this: *RSC Adv.*, 2022, **12**, 62

Catalytic activity, thermal stability and structural evolution of PdCu single-atom alloy catalysts: the effects of size and morphology

Qing Liu,[ab] Xiaoxu Wang,[c] Lu Li,[ab] Keke Song,*[ab] Yanzhou Wang[ab] and Ping Qian *[ab]

Received 13th October 2021
Accepted 2nd December 2021

DOI: 10.1039/d1ra07581k

rsc.li/rsc-advances

Single-atom alloys (SAAs) have been emerging as an important field of research in electrocatalysis owing to extremely high atom utilization, unique structure and high catalytic activity. In this work, the catalytic properties and thermal stability of PdCu SAAs with a crown-jewel (CJ) structure are studied by density functional theory (DFT) calculations and the molecular dynamics (MD) simulation method. The DFT results reveal that CJ-structured PdCu SAAs show excellent HER and ORR catalytic performance, and can be regarded as a promising alternative to Pt catalysts towards the ORR or HER. Additionally, we attempt to explain the high catalytic activity of PdCu SAAs by electronic structure analysis. In addition, MD simulation results confirm the thermal stability of CJ-structured PdCu. More importantly, we found that CJ-structured PdCu clusters undergo a structural transformation from cuboctahedral (Cubo) to icosahedral (Ico) structure by heating or after the adsorption of reaction intermediate, which indicates that Cubo is less stable than the Ico structure. Besides, Cubo–Ico transformation is size-dependent and only found in small clusters. Furthermore, the effects of size and morphology on melting properties are discussed. The melting point increases as cluster size increases, which agrees well with Pawlow's law.

1. Introduction

Metallic nanoclusters (NCs) have received great attention in materials science and engineering for their excellent properties owing to their small size and large surface-volume ratio.[1,2] Bimetallic nanoclusters exhibit enhanced and more complex properties than the corresponding monometallic components attributed to the synergistic effect of the different elements.[3,4] By tuning their size, structures, and chemical compositions as well as the surface state properties, the unique properties of bimetallic NCs can be utilized in a large range of fields, especially in heterogeneous catalysis.[5,6] With regard to electrocatalysis, much effort has been dedicated to improving the catalytic performance of nanoalloys by designing different kinds of structures. Some special structural models of NCs, such as core–shell,[7,8] onion-like,[9] quasi-janus structures[10] and crown-jewel (CJ) structures[11,12] have been found to have structure-dependent properties and are an important focus of nanostructure research. Specifically, CJ-structured bimetallic NCs, where the one metal clusters serve as the crowns and another metal atoms serve as jewels decorating the special positions of the crowns, which is regarded as one kind of single-atom-alloy (SAA). SAA contains isolated metal atoms singly dispersed on the surface of a host metal, which turns out to a research frontier in heterogeneous catalysis.[13–15] SAAs show extremely high atom utilization efficiency, which is especially beneficial to precious metal catalysts. It is reported that when the size of cluster is about 9.03 nm, the cluster can efficiently represent the properties of bulk metal surface.[5] However, not only the metal surface, but metal clusters can also be the supports. Comparable clusters with the dispersions of isolated noble metal atoms have been prepared and applied in catalysis experimentally. It is reported that SAAs with CJ structure exhibit excellent catalytic property, compared to conventional nanocluster catalysts.[11,12,16] For example, Zhang *et al.* have prepared crown-jewel-structured AuPd nanocluster by a galvanic replacement reaction method, which located Au single atoms at the top position of Pd host clusters. This single atom structure showed markedly high catalytic activity for aerobic glucose oxidation.[12] Besides, AuPd single atom structures were also prepared toward oxygen reduction reaction. It was showed that discrete Pd single atoms dispersed in Au nanocluster surfaces will significantly improve reactivity of the surface toward H_2O_2 production.[16] In addition, Zhang *et al.* prepared the colloidal SAAs of "crown jewel" structured (IrPd)/Au nanoclusters and found that this SAAs were the most effective catalysts for aerobic glucose oxidation tested to date.[11] The unique electronic structure and coordinative unsaturation of the active sites for CJ structure modify the adsorption properties of intermediates,

[a]*Beijing Advanced Innovation Center for Materials Genome Engineering, University of Science and Technology Beijing, Beijing, 100083, China. E-mail: qianping@ustb.edu.cn; KeKSong@163.com*

[b]*Department of Physics, University of Science and Technology Beijing, Beijing, 100083, China*

[c]*DP Technology, Beijing, 100080, China*

and thus significantly enhances the catalytic performance of CJ. Additionally, the strength of metal bonds between single atoms and host metal results in the high stability of CJ systems.[17] Thus, SAAs catalysts with CJ structure are worth studying deeply as an attractive candidate for the catalytic applications.

Pt-based materials have been long known as the most efficient metal catalysts for many conventional chemical reactions, especially for oxygen reduction reaction (ORR) and hydrogen evolution reaction (HER). However, deficiencies such as high cost and scarcity hamper their large-scale industrial application. Thus, searching Pt-free alternatives has been an important focus on the design of advanced electrocatalysts. Especially, Pd-based nanoalloy is an attractive alternative to Pt in electrocatalytic materials since Pd has similar physicochemical characteristics with Pt. In recent years, it has become common to alloy Pd with non-noble transition metals (*e.g.* Fe, Co, Ni, Cu, W) to design advanced catalysts.[18–21] In this regard, compared with other transition metals, Cu is cheap and highly abundant, which will significantly reduce the high cost of precious metal catalysts. Besides, it has reported that Pd alloyed with Cu achieved high catalytic activity for both ORR and HER owing to strong synergistic effect.[22–24] For example, Tang *et al.* investigated the effect of alloy composition on the oxygen reduction activity of PdCu nanoparticles. They found that the average oxygen binding reduced when Cu is added to Pd, indicating an increase in catalytic activity up to a peak at 1 : 1 Pd/Cu ratio.[25] Besides, Zhang *et al.* prepared monodispersed bimetallic PdCu nanoparticles. They found that both the HER activity and stability of PdCu/C are highly dependent on the Pd/Cu atomic ratios.[22] Zhang *et al.* synthesized CuPd nanocrystals with a variety of nonspherical shapes and found that the ORR activity is remarkably shape-dependent.[26]

As the CJ-structured SAA is emerging as an important field of research in catalysis, it seems interesting and challengeable to investigate PdCu nanoalloys with the CJ structure, which may possess excellent catalytic activity and could be a promising alternative to Pt catalysts. However, the detailed investigations about structural properties and catalytic properties towards ORR and HER of CJ-structured PdCu nanoclusters are still scarce, which are important for their potential application in catalysis.

In recent years, density functional theory (DFT) calculations and molecular dynamics (MD) simulation method, are playing an increasingly important role in studying nanostructure and predicting material properties.[27–31] Herein, our work is mainly consisted of two parts: the study of catalytic properties towards ORR and HER and thermal stability of CJ-structured PdCu SAAs. The thermal stability is an important property for CJ-structured nanoclusters to function as a catalyst. The catalyst will not be able to work if the thermal stability is poor. Besides, the melting point is strongly linked with the thermal stability of the clusters. Generally, the more stable of the cluster, the higher the melting point. Thus, the study of melting behaviors is important for CJ-structured nanocluster for the catalytic applications. By DFT calculations, we explore the catalytic activity of PdCu SAAs toward ORR and HER, respectively. On the other hand, MD simulations based on the EAM potential are used to investigate the melting properties and structural evolution of PdCu nanoclusters during heating process. Moreover, a structural transformation from cuboctahedral (Cubo) to icosahedral (Ico) structure is observed by heating or after the adsorption of intermediates. The Pawlow's law is also observed in CJ structure. Besides, the effects of the morphology and size on these properties are also discussed.

2. Computational methods and models

2.1. DFT calculations

The DFT calculations are performed using the Vienna *Ab initio* Simulation Package (VASP).[32] The generalized gradient approximation (GGA) of Perdew–Burke–Ernzerhof (PBE) is applied to describe the electron exchange-correlation energy.[33] The ion–electron interactions are described by the projector augmented wave (PAW) method.[34] Plane-wave expansions are set with a kinetic energy cutoff of 500 eV. The Brillouin zone is sampled with a gamma ($1 \times 1 \times 1$) point. A 25.0 Å cubic supercell is composed of a PdCu nanocluster with an enough large vacuum space to separates the NC from its periodic image. The atomic structure is optimized with the energy converged to 1.0×10^{-4} eV and the force converged to 0.01 eV $Å^{-1}$.

We calculate the change in Gibbs free energy (ΔG) for ORR and HER pathways on PdCu systems, which is defined as $\Delta G = \Delta E + \Delta E_{ZPE} - T\Delta S$, where ΔE is the total energy change of the reaction obtained from DFT calculations, ΔE_{ZPE} and ΔS are the changes in zero-point energy and the entropy between the adsorbed state and the gas phase, respectively. T is temperature (298.15 K, in this work). Zero-point energies and S corrections are calculated from the vibrational frequencies in the harmonic oscillator approximation as done by Peterson *et al.*[35] Besides, the adsorption energy of an adsorbate (ΔE_{ads}) on nanoclusters are defined as: $E_{ads} = E_{cluster + adsorbate} - E_{cluster} - E_{adsorbate}$, where $E_{cluster + adsorbate}$ is the total energy of metal nanoclusters with an adsorbate, $E_{cluster}$ is the energy of the nanocluster, and $E_{adsorbate}$ is the energy of an isolated adsorbate species, respectively.

The free energies of the ORR elementary reactions are calculated based on a computational standard hydrogen electrode (SHE) model proposed by Nørskov *et al.*[36] This model defines that the free energy of a proton/electron pair ($H^+ + e^-$) in solution is equal to half of the free energy of H_2 molecule. Besides, the effect of external bias on the reaction can be applied by shifting ΔG by $-neU$, where e is the transferred charge and U is the applied electrode potential, and n is the number of proton–electron transfer pairs. The effects of pH value can be treated as an energy shift to free energy change: $\Delta G_{pH} = -k_B T \ln 10 \times pH$ and pH is assumed to be zero for acidic medium in this work.

2.2. MD simulation

Molecular dynamics simulations using the Large-scale Atomic/Molecular Massively Parallel Simulator (LAMMPS) software[37] are performed to study the heating process at the atomistic level of PdCu CJ nanoalloys. The interaction between metal atoms is

described based on the embedded atom method (EAM). The EAM, developed by Zhou *et al.*, is described with the identical analytic form and has been extended to enable calculations of alloys with any combination of 16 metals.[38] The detailed description of this potential function used in this study is given in previous papers.[39] Besides, this EAM potential has been successfully used in describing thermodynamic properties of metal nanoclusters and nanoalloys.[40,41] In MD simulation, the temperature is controlled by the Nosé–Hoover thermostat. The equations of motion are integrated using Verlet leapfrog algorithm and the time step is set to 1 fs. The heating processes of alloy clusters are simulated as follows: firstly, the nanoclusters are fully relaxed at 0 K to reach a minimum energy configuration. Then, the clusters are heated up from 0 K to 1600 K (which is above the melting pointing of the alloy nanoclusters) with a temperature increment of 20 K, each with 240 ps equilibrated simulation time. In this work, the melting properties and structural evolution of PdCu SAA nanoclusters are studied by MD simulations.

2.3. Models of CJ-structured PdCu nanoclusters

In this work, we conduct an investigation into the catalytic property and thermal stability of CJ-structured PdCu SAAs with different morphologies and cluster sizes. It is known that clusters with certain special numbers of atoms are much more abundant than others when generated in typical cluster experiments, and these numbers are called geometric "magic numbers".[42] For metal nanoclusters, the relative stable geometries are normally those consisting of a magic number N of atoms (N = 55, 147, 309, 561, 923, *etc.*),[43,44] which normally corresponds to highly symmetric structures, such as icosahedral and cuboctahedral models. The highly symmetric structures Cubo and Ico are the most commonly used structural models for the nanocluster research, experimentally and theoretically.[45–47] Therefore, closed atomic shell structures of Ico and Cubo models including the magic number of atoms are used as host cluster in this work. For PdCu nanoclusters, all vertices of Cu clusters are replaced by Pd atoms, where the Cu clusters act as the host cluster (crowns) and Pd atoms serve as jewels decorating the vertex positions of the crowns, corresponding to the typical CJ structure. To study the size effect, PdCu nanoclusters with sizes of 55, 147, 309, 561 and 923 atoms are used. Fig. 1a and b displays our model system of CJ-structured PdCu nanoclusters with Cubo and Ico morphologies. In this work, the catalytic properties are studied based on DFT calculations. Besides, thermal stability and structural evolution of PdCu SAA structures during heating are investigated by MD simulation.

3. Results and discussion

3.1. Catalytic properties

In this section, we investigate the HER and ORR catalytic properties on PdCu SAAs, respectively, by the DFT calculations. For the catalytic property researches, two morphologies are considered, that is the highly symmetric Cubo, and Ico structures. Besides, size effects are also discussed and the PdCu nanoclusters with sizes of 55 and 147 atoms are selected.

3.1.1. HER catalytic activity. It is reported that the Gibbs free energy of hydrogen adsorption, ΔG_H, is a good activity descriptor to evaluate the HER catalytic activity.[48,49] The free energy for adsorbed hydrogen is defined as $\Delta G_{H^*} = \Delta E_{H^*} + \Delta E_{ZPE} - T\Delta S_H$, where ΔE_{ZPE} and ΔS are the changes in zero-point energy and entropy between the adsorbed state and gas-phase state of hydrogen, respectively, T is temperature. ΔE_{H^*} is the hydrogen adsorption energy based on DFT calculation. The ideal HER catalyst has zero ΔG_{H^*} to achieve optimal catalytic activity, which is a good compromise between hydrogen adsorption and the subsequent desorption.[50] This indicates that the smaller the value $|\Delta G_{H^*}|$ is, the better HER performance of the catalyst will be.

To investigate the effect of the addition of single atom Pd on HER or ORR catalytic activity of CJ-structured PdCu nanoclusters, three equivalent adsorption sites according to the Pd-centered symmetry for Ico configuration (T1, B1, H1 sites) and four adsorption sites for Cubo configuration (T1, B1, H1 and H2 sites) are considered, as shown in Fig. 1c and d. The adsorption energy of H atom (E_{H^*}) on PdCu clusters with Ico and Cubo structures at different adsorption sites are calculated. For comparison, the hydrogen adsorption of Pt and Pd clusters are also calculated. The most favorable adsorption energies and adsorption sites for hydrogen atom are listed in Table 1. It is seen that the hydrogen adsorption energies for these systems are all negative, indicating that hydrogen adsorption is energetically favorable. Besides, the calculated Gibbs free energy diagram of hydrogen evolution of PdCu, Pt and Pd nanoclusters

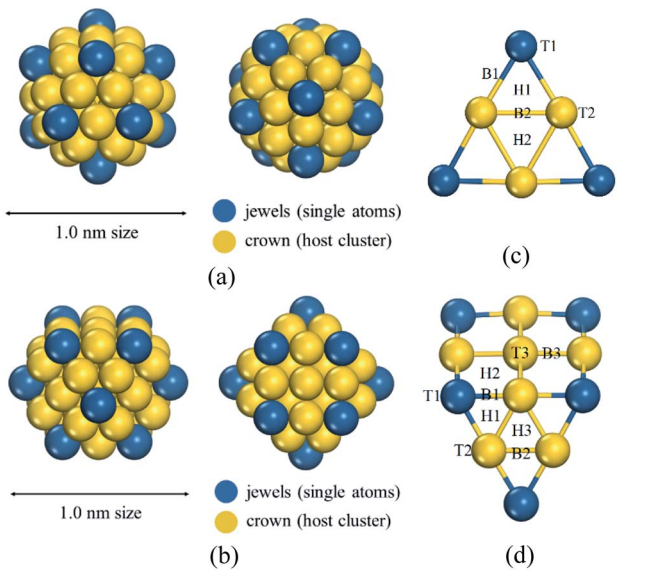

Fig. 1 Schematic models of crown jewels (CJ) systems with (a) Ico and (b) Cubo structures. The blue spheres represent jewels (single atoms) and the yellow metal cluster represent the crown (host cluster). The jewels (single atoms) decorate the vertex sites of the crown (host cluster). In this work, single atoms refer to Pd atoms, host cluster refers to Cu cluster. Besides, the possible adsorption sites of 55-atom PdCu clusters for (c) Ico and (d) Cubo.

Table 1 The hydrogen adsorption energies (E_{H*}) and Gibbs free energy ΔG_H at most stable adsorption sites for PdCu, Pt and Pd nanoclusters

Cluster	Configuration	Adsorption site	E_{H*} (eV)	ΔG_H (eV)
$Pd_{12}Cu_{43}$	Ico	H1	−0.34	−0.10
$Pd_{12}Cu_{43}$	Cubo	—	—	—
$Pd_{12}Cu_{135}$	Ico	H1	−0.26	−0.02
$Pd_{12}Cu_{135}$	Cubo	—	—	—
Pd_{55}	Ico	H1	−0.66	−0.42
Pd_{55}	Cubo	H1	−0.56	−0.32
Pt_{55}	Ico	B1	−0.82	−0.58
Pt_{55}	Cubo	B1	−0.75	−0.51
Pt_{147}	Ico	B1	−0.63	−0.39

are displayed in Fig. 2c. Theoretically, the overall HER reaction can be described by a three-state diagram consisting of an initial H^+ state, an intermediate H* state and the final product $1/2H_2$, as seen in the figure.

From the figure we can draw the following conclusions: firstly, when Pd single atoms embedded in Cu nanocluster surface, the $|\Delta G_{H*}|$ of this SAAs is smaller than Pd and even Pt catalysts, indicating that CJ-structured PdCu shows better HER activity. Thus, CJ-structured PdCu catalyst is promising to realize highly efficient and low-cost electrocatalytic H_2 production. Secondly, we found that the HER activity of Pd clusters with Ico and Cubo configurations are both higher than Pt clusters. Thirdly, catalysts with Cubo configuration for both Pd and Pt clusters have better HER catalytic performance than that with Ico configuration.

In addition, we are surprised to find a ligand-induced structural evolution for $Pd_{12}Cu_{43}$ cluster with Cubo. $Pd_{12}Cu_{43}$ cluster with Cubo structure transforms into Ico structure after adsorbed H atom on cluster surface, as seen in Fig. 2a. Besides, the total energy of the adsorption system which transformed into icosahedral is almost the same with that of icosahedral adsorption system. This structure transformation indicates that Cubo structure is metastable structure and less stable than Ico. For example, $Pd_{12}Cu_{43}$–Cubo structure is less stable than that icosahedral structure by −4.07 eV. The similar ligand-induced structural transformation is also found in Pt_{55} cluster. It is reported that Pt_{55} cluster undergo a structural evolution from Cubo to an Ico structure by the Mackay transformation with the help of the adsorption of methylamine.[51] Cubo–Ico transformation is driven by a combination of both the external forces resulting from the adsorption of the ligand, which pull out the Pt atoms on the surface of NCs in a radial direction, and the contraction forces in a tangential direction.

To elucidate the excellent catalytic property of PdCu SAA structure, we take $Pd_{12}Cu_{43}$ SAA as a representative and we calculate the electronic structure. It is known that the high catalytic activity of SAA is attributed not only to the unique structure, but also to the electronic structure of single atom. Bader analysis is used to quantify the charge changes around each atom in PdCu SAA structure.[52] The Bader charges change of some atoms for $Pd_{12}Cu_{43}$ SAA and Pd_{55} cluster are shown in the Fig. 2d and e. For Pd_{55} cluster, we see that vertex Pd atoms are weakly negatively charged. However, when Pd single atoms embedded in Cu nanocluster, the negative charge density of single Pd atoms significantly increases and Cu atoms are all

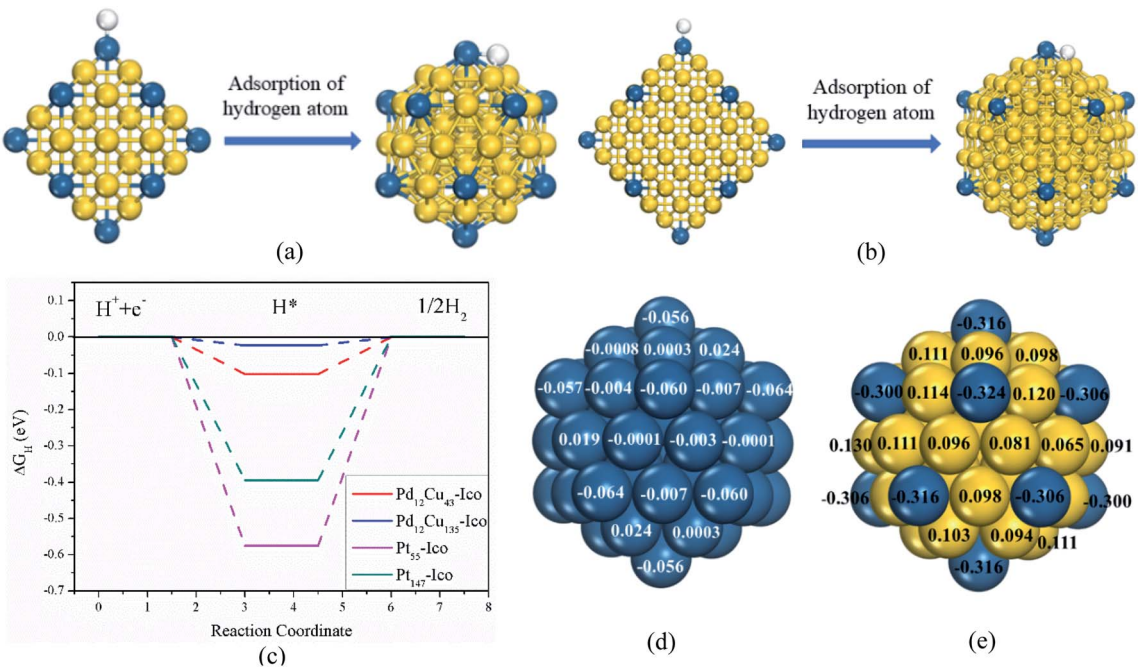

Fig. 2 The Cubo–Ico structural transformation of (a) $Pd_{12}Cu_{43}$ and (b) $Pd_{12}Cu_{135}$ clusters after the adsorption of hydrogen atom; (c) the calculated Gibbs free energy diagram of hydrogen evolution for PdCu, Pt and Pd nanoclusters. DFT calculations of electronic structure of (d) Pd_{55} and (e) $Pd_{12}Cu_{43}$ clusters.

Table 2 Most favorable adsorption energy of oxygen atom and adsorption sites, ORR RDS and overpotential on PdCu, Pt and Pd nanoclusters with varying size and morphology

Structures	E_{O*} (eV)	Adsorption site	RDS	Overpotential (V)
$Pd_{12}Cu_{43}$-Ico	−4.73	H1	R4	0.87
Pd_{55}-Ico	−4.55	H1	R3	0.81
Pt_{55}-Ico	−4.50	H1	R4	0.78
Pt_{55}-Cubo	−4.55	B1	R4	0.88
$Pd_{12}Cu_{135}$-Ico	−4.38	H1	R3	0.67
Pd_{147}-Ico	−4.41	H1	R3	0.74
Pt_{147}-Ico	−4.38	H1	R4	0.65

positively charged. This is attributed to electron transfer from the surrounding Cu atoms to single Pd atoms. This similar results are also found in AuPd[12] and (IrPd)/Au.[11] The anionic charge on vertex Pd atoms may act as catalytically active sites for HER. Thus, the negatively charged Pd single atoms maybe the cause for the high catalytic performance of PdCu SAA catalyst.

3.1.2. ORR catalytic activity. In this section, we study the adsorption properties of ORR intermediates and explore the oxygen reduction pathways on PdCu SAAs. In general, the adsorption strength of O atom is commonly used as effective descriptor of the ORR activity. Nørskov and co-workers proposed a volcano-shaped correlation between the oxygen adsorption energy and ORR activity.[36] The adsorption energy of O atom (E_{O*}) with varying size (55 and 147 atoms) and morphologies (Ico and Cubo) are calculated, as shown in Table 2. For comparison, the adsorption energy of Pt and Pd nanoclusters are also presented. For reference, the E_{O*} of Pt_{147} cluster with Ico is −4.38 eV, which agrees well with the previously reported results ($E_{O*} = -4.35$ eV),[53] which confirms the accuracy of our calculation for adsorption property of metals nanoclusters.

As shown in the Table 2, we can see that the O adsorption energy of $Pd_{12}Cu_{43}$ SAAs with Ico is slightly stronger than Pt_{55} and Pd_{55} clusters, regretfully, which means that ORR activity of $Pd_{12}Cu_{43}$ may be lower than Pd and Pt clusters. However, when PdCu cluster size increases to 147 atoms, the E_{O*} of $Pd_{12}Cu_{135}$-ico is weaker than Pd_{147}-ico cluster and close to Pt_{147}-ico cluster, indicating that PdCu with 147 atoms may show better ORR activity than Pd cluster and is even comparable to Pt cluster. Thus, CJ-structured PdCu can be considered as a promising ORR catalyst with low cost. Besides, we also see that the O adsorption energy of Pt_{55} with Cubo is stronger than that with Ico structure. This indicates that the Ico morphology may have higher ORR catalytic activity than Cubo. Furthermore, a ligand-induced structural transformation is also found. As shown in Fig. 3a and c, $Pd_{12}Cu_{43}$ cluster with Cubo structure transforms into Ico structure with the help of the adsorption of ORR intermediates: O and OH species on cluster surface. This further confirms that Cubo is less stable than Ico structure.

To further study the ORR catalytic performance of CJ-structured PdCu nanoclusters, we calculate the Gibbs free energy diagram, which are used to explore the energetics of ORR elementary steps. In general, for alloy nanoclusters and SAA structures,[54–56] ORR prefer to proceed through the associative mechanism in acid media. The associative pathway of ORR at the PEMFC cathode is described by the following four elementary steps:

$$O_2(g) + H^+ + e^- + * \rightarrow *OOH$$

$$*OOH + H^+ + e^- \rightarrow *O + H_2O(l)$$

$$*O + H^+ + e^- \rightarrow *OH$$

$$*OH + H^+ + e^- \rightarrow H_2O(l) + *$$

where * denotes an adsorption site on the surface. The free energy diagrams of the ORR associative pathway occurring on $Pd_{12}Cu_{43}$ and $Pd_{12}Cu_{135}$ clusters with Ico at 0 V and at 1.23 V are shown in Fig. 4. Initially, the adsorbed O_2 can be easily

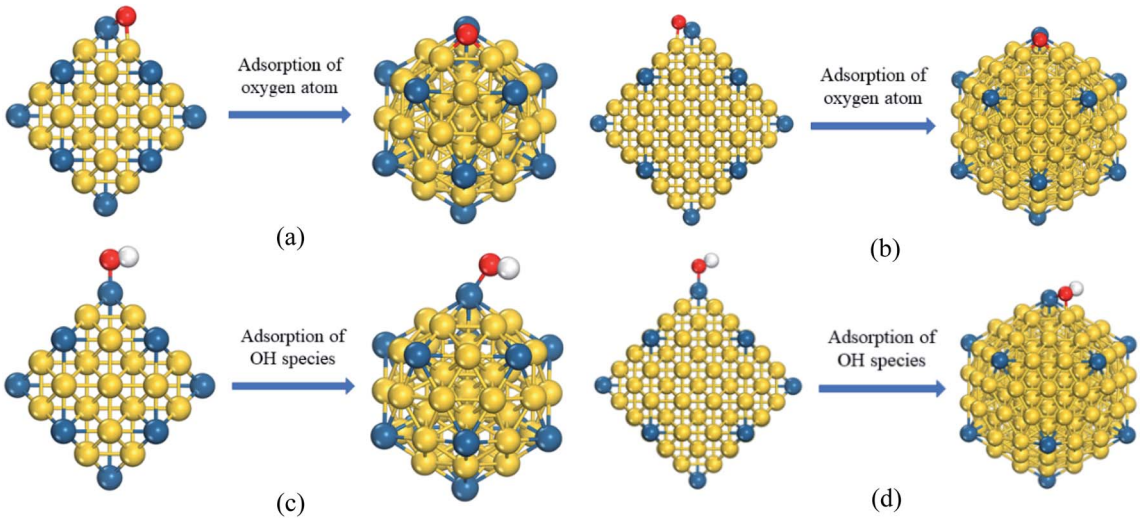

Fig. 3 The Cubo–Ico structural transformation of (a) $Pd_{12}Cu_{43}$ and (b) $Pd_{12}Cu_{135}$ clusters after the adsorption of oxygen atom; (c) $Pd_{12}Cu_{43}$ and (d) $Pd_{12}Cu_{135}$ clusters after the adsorption of OH species.

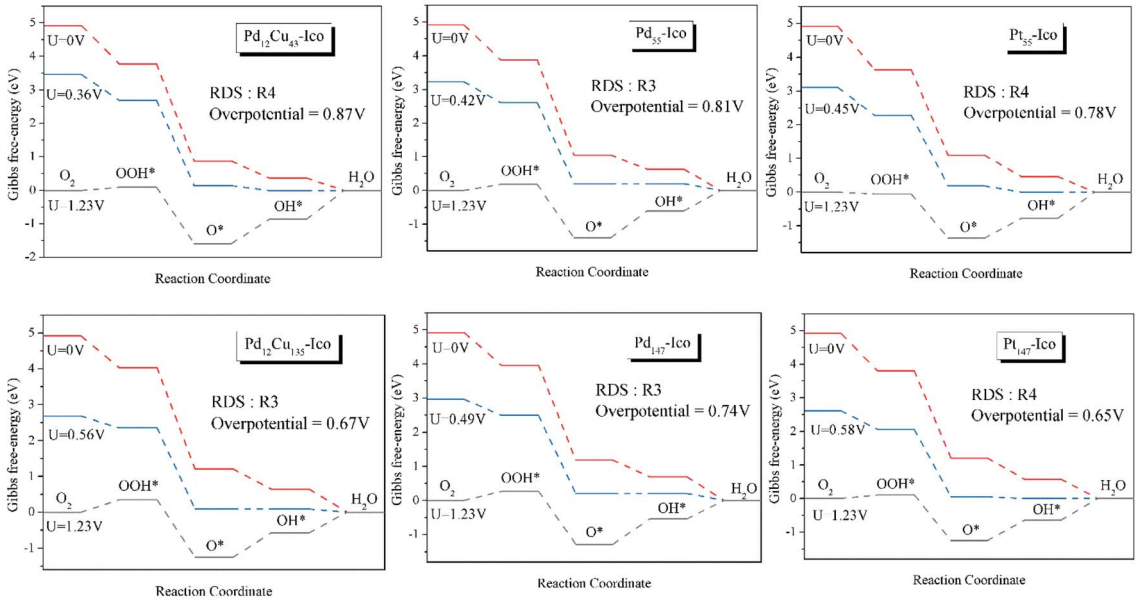

Fig. 4 The Gibbs free energy diagrams of the ORR pathway occurring on CJ-structured PdCu, Pt and Pd clusters at 0 V, at 1.23 V and at the limiting potential.

hydrogenated by adsorbing a proton coupled with an electron and forms an OOH* species. For $Pd_{12}Cu_{43}$-ico cluster, this process is downhill in the free energy profile by 1.14 eV. Subsequently, OOH* will be further hydrogenated with the help of a proton and one electron, forming the O* species and one H_2O molecule. The free energy in the first H_2O formation step is downhill by 2.91 eV. Next, the remaining O* species will be further hydrogenated to form an OH* species and this step is also downhill in the free energy profile by 0.50 eV. Finally, the second H_2O molecule can be formed when the OH* species reacts with a proton coupled with one electron transfer. In this hydrogenation process, the Gibbs free energy decreases by 0.36 eV. The reaction pathway is overall downhill at zero potential, indicating that all the ORR steps proceed spontaneously on these catalysts from the viewpoint of thermodynamics. As the potential shifts to the ORR equilibrium potential ($U = 1.23$ V), one or more of elementary steps become uphill and less energetically favorable. The step corresponding to the most positive free energy at 1.23 eV is the most energetically unfavorable and most likely determines the entire reaction rate, which turns out to be the rate-determining step (RDS). The ORR overpotential is defined as the free energy corresponding to the highest endothermic step ΔG_{max} at 1.23 V divided by e, which is an important criterion to evaluate the ORR catalytic performance and search for promising ORR catalysts. Obviously, for $Pd_{12}Cu_{43}$-Ico cluster, step from OH* to second H_2O formation is RDS, the overpotential is 0.87 V. Similarly, the rate-determining step of $Pd_{12}Cu_{135}$-Ico lies in step from O* to OH*, with overpotential values of 0.67 V. Besides, the overpotential values and RDS of PdCu, Pd and Pt clusters are listed in Table 2. The low overpotential value of CJ-structured $Pd_{12}Cu_{135}$ SAA indicates that it exhibits a higher ORR activity than Pd_{147} cluster and is comparable to Pt_{147} cluster, which is consistent with E_{O*} results. In addition, we compared the ORR overpotential of CJ-structured PdCu SAAs with those previously reported Pt-based nanoclusters. For example, core–shell nanoclusters consisting of 12 different 3d–5d transition metal cores (groups 8–11) and a Pt shell, which with overpotential values of 0.72–1.04 V,[57] and M@Pt core–shell clusters (M represents 3d transition metal), which with values of 0.61–1.5 V.[58] We can see that the ORR overpotentials of PdCu are lower than those Pt-based nanoclusters. Besides, we found the overpotential of CJ-structured PdCu is also lower than the graphene-supported Pt nanocluster (ranging from 0.69 to 1.68 eV).[59] The above means that PdCu SAAs exhibit better ORR activity than those Pt-based nanoclusters.

However, the overpotentials of PdCu SAAs are slightly larger than state-of-the-art ORR catalyst, for example, Pt(111) (~0.45 V)[36] and 2D-supported SACs (~0.55 V).[60] Although the overpotentials of PdCu clusters are not comparable to state-of-the-art ORR catalyst, CJ-structured cluster catalysts still show several major advantages over those ORR catalysts. Firstly, Cu cluster as host cluster reduces the usage of precious metals and will significantly reduce production costs. Secondly, the strength of metal bonds between single atoms and host metal ensure that CJ systems are often more stable than oxide-supported or 2D-supported SACs. Thirdly, the nanoclusters with more uniform particle sizes can be obtained in the dispersed systems compared with those in the supported cases, especially under conditions of a high metal concentration, because the dispersed metal nanoclusters can be easily concentrated by evaporating the solvent without changing the structures.[61] Thus, CJ-structured PdCu cluster can be considered as a promising ORR catalyst with low cost for fuel cells cathode applications.

3.1.3. Size effect. From Table 1, we found that the CJ-structured $Pd_{12}Cu_{135}$ cluster has smaller $|\Delta G_{H*}|$ than that with

55 atoms, meaning that HER activity is improved as the cluster size increases. It should be noted that $Pd_{12}Cu_{135}$ with Ico has $|\Delta G_{H^*}|$ value of 0.02 close to zero, which indicates very excellent HER performance. In addition, from the Table 2, we can see that the ORR catalytic activity of CJ-structured PdCu with 147 atoms is higher than that with 55 atoms due to its low overpotential and low E_{O^*}. Besides, Pt and Pd clusters with 147 atoms also show better ORR catalytic property than that with 55 atoms, respectively. Therefore, we conclude that the size has an important impact on adsorption strength of intermediate and catalytic properties, thus ORR and HER catalytic activity of PdCu SAAs can be further improved by adjusting cluster size.

Moreover, the structural transformations from the Cubo structure to Ico structure are also found for CJ-structured PdCu clusters with 147 atoms when O (seen Fig. 3b), OH species (Fig. 3d) or H atom (Fig. 2b) are adsorbed on the cluster surface. This indicates that CJ-structured $Pd_{12}Cu_{135}$ SAA with Cubo is also a metastable structure.

3.2. Melting properties

In this section, the heating process for PdCu nanoclusters is studied by MD simulation with the embedded atom method, in hope to explore the effects of morphology and cluster size on the thermodynamic stability and structural evolution during heating. Fig. 6a–c shows the temperature dependence of total potential energy (PE) during heating for various sizes (147, 309, 561, 923 atoms) and morphologies (cuboctahedral and icosahedral structures) of CJ-structured PdCu SAAs. We can see that there is a sharp jump at about 800 K for $Pd_{12}Cu_{135}$ clusters both with Ico and Cubo configurations, which corresponds to the melting point. Besides, we found that $Pd_{12}Cu_{135}$ with Cubo structure undergo a solid–solid structural transformation from Cubo to Ico structure at 0 K (the snapshot images near the structural transformation point are shown in the inset), which indicates that Cubo is less stable than Ico. This conclusion is consistent with the ligand-induced structural transformation results mentioned earlier. From the potential energy curve of $Pd_{12}Cu_{297}$-Cubo, we see that apart from the melting point with 846 K, $Pd_{12}Cu_{297}$ with Cubo structure also shows a cuboctahedral to icosahedral (Cubo to Ico) structure transformation at 320 K with a sharp drop in potential energy. However, when the cluster size increases to 561 and 923 atoms, the Cubo–Ico structural transformation phenomenon disappears, which indicates that Cubo–Ico transformation is size-dependent and occurs only for small nanoclusters.

The radial distribution function (RDF) is commonly used to study the structural evolution and the degree of disordering of the nanostructure. The RDF is defined as the probability of finding a pair of atoms with a distance r, relative to the probability expected for a completely random distribution, compared with a homogeneous distribution.[62,63] We take $Pd_{12}Cu_{297}$ SAA with Cubo as an example, total RDFs at 100 K (before Cubo–Ico structural transformation), 320 K (at Cubo–Ico transformation point), 500 K, 700 K, 800 K and 850 K (near the melting point) are shown in Fig. 5. The corresponding structural evolution snapshots at different temperatures during heating are depicted in the inset. We see that the RDFs show sharp peaks at 100 K, which corresponds to a regular cuboctahedral structure. When it is heated up to 320 K, the RDF peaks suddenly change and exhibit the main structural characteristics of an icosahedral structure, which is attributed to the Cubo–Ico structural transformation. When it comes to 500 K, 700 K and 800 K, the RDF peaks gradually become smaller and broader, indicating that the icosahedral structure becomes more disordered. The peak intensity is getting weaker as the temperature increases. When the temperature reaches melting point 850 K, the long-range order characteristic lost in RDF, suggesting the characteristic of amorphous liquid structure. Besides, we observe that Pd single atoms still stay at the original vertex sites until the melting point and the CJ structure is well maintained, which proves the thermal stability of PdCu SAA.

In addition, the Cubo–Ico transformation temperature and melting points of CJ-structured PdCu SAAs changing with the different cluster sizes and morphologies are listed in Table 3. We found that the melting point of PdCu with Ico structures is higher than that with Cubo structure for each cluster size, which further confirms that Ico structure of PdCu is more stable

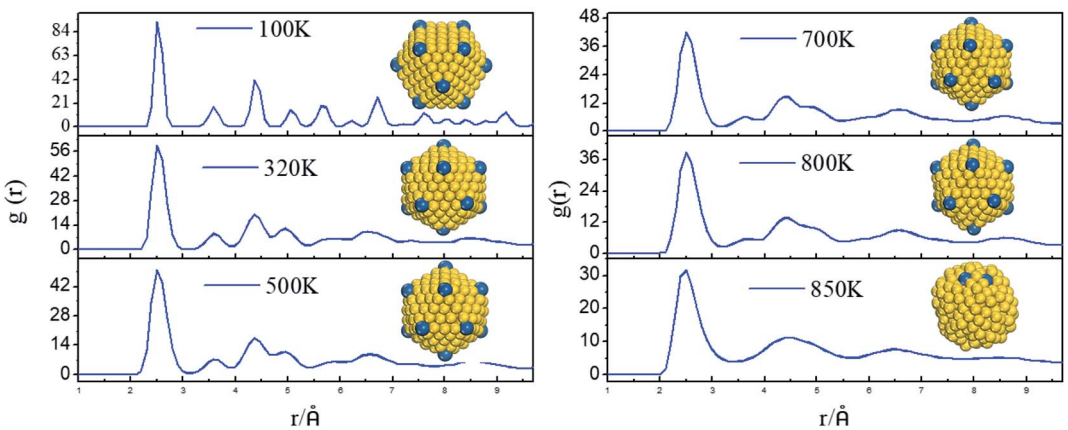

Fig. 5 Total RDFs for CJ-structured $Pd_{12}Cu_{297}$ SAA with Cubo at different temperatures during heating. Inset: the corresponding structural evolution snapshot at different temperatures.

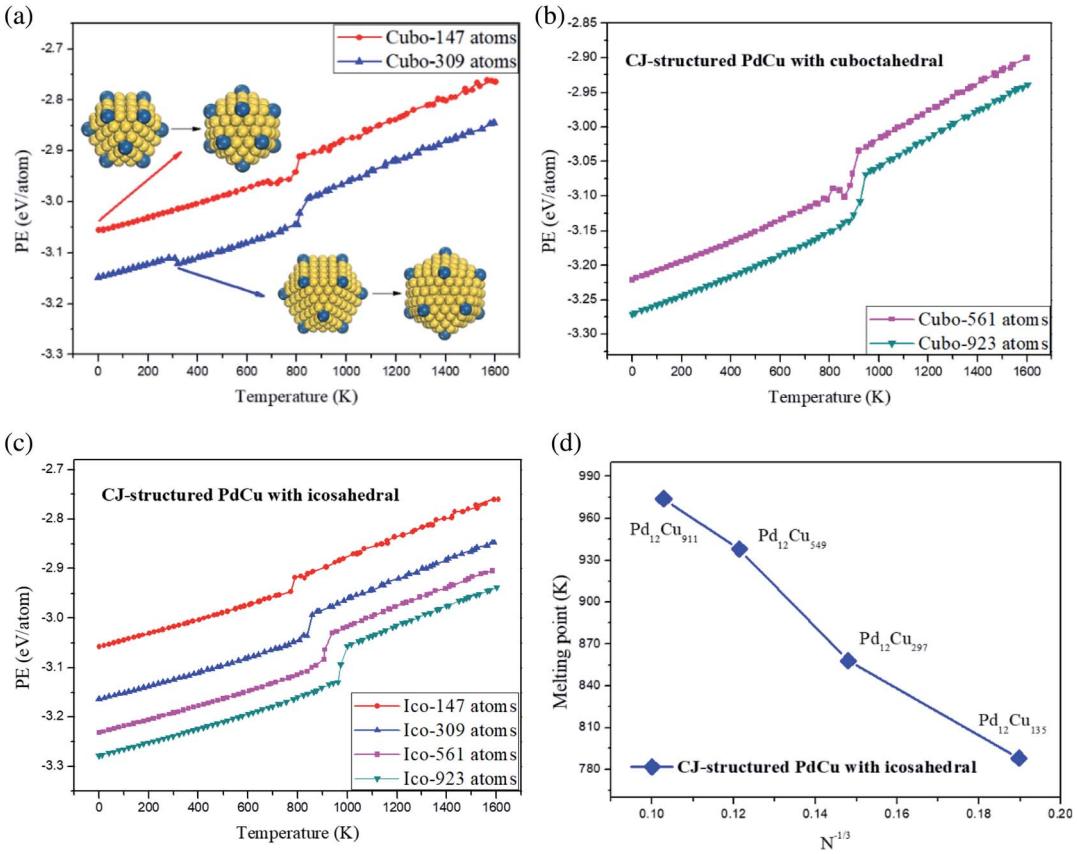

Fig. 6 (a) The temperature dependence of PE during heating for a CJ-structured PdCu–Cubo with 147 and 309 atoms; (b) PdCu–Cubo with 561 and 923 atoms; (c) PdCu with Ico structures; (d) the melting point of PdCu SAAs *versus* $N^{-1/3}$.

Table 3 The Cubo–Ico transformation temperature (T_{tran}) of Cubo structures, and the melting points (T_{melt}) of CJ-structured PdCu SAAs with the different cluster sizes and morphologies

Structure	T_{tran} (K)	T_{melt} (K)	Structure	T_{melt} (K)
Cubo-147	0	812	Ico-147	788
Cubo-309	320	846	Ico-309	858
Cubo-561	—	918	Ico-561	938
Cubo-923	—	947	Ico-923	974

than Cubo. For different sizes, the melting point of CJ-structured PdCu nanoclusters increases as the cluster size increases and the melting points of Ico configurations against $N^{-1/3}$ (N is total number of atoms in PdCu icosahedral cluster) are plotted in Fig. 6d. The melting point of Ico correlates linearly with $N^{-1/3}$, which agrees well with Pawlow's law.[64]

4. Conclusions

In this work, the HER and ORR catalytic activity and thermal stability of CJ-structured PdCu SAAs are studied by using DFT calculations and MD simulation, respectively. The effects of the morphology and size on these properties are discussed. For the catalytic property, we found that CJ-PdCu show higher HER catalytic activity than the state-of-the-art Pt catalysts, which can be considered as low cost and highly efficient HER electrocatalysts for H_2 production. On the other hand, by calculating the adsorption energy of oxygen atom and Gibbs free energy diagram, we found that PdCu SAA also exhibits a higher ORR activity than Pd cluster and comparable activity to Pt cluster. Thus, CJ-structured PdCu SAA can also be used as ORR catalysts for fuel cells cathode applications. Besides, size effects are also discussed and HER and ORR catalytic performance both improve as cluster size increases. In addition, MD simulation proved the thermal stability of CJ-structured PdCu and PdCu SAA structure can still be stable during heating until melting. Furthermore, a structural transformation from Cubo to Ico structure is found by heating or the adsorption of reaction intermediates. For example, DFT results show that CJ-structured PdCu clusters of 55 and 147 atoms both undergo structural evolution from Cubo to Ico structure after the adsorption of reaction intermediates. On the other hand, MD simulations show that PdCu SAA of Cubo structure transform into Ico during heating process and this structural transformation occurs before melting point. Besides, the effects of the morphology and size on melting properties are also discussed. Our results demonstrate the potential applications of SAAs with CJ structure in catalysis. The catalytic activity and thermal stability of CJ-structured PdCu nanoalloys can be tuned

by the size and morphology, which provides a guidance for the rational design of SAA for catalytic applications.

Conflicts of interest

There are no conflicts to declare.

Acknowledgements

This work was financially supported by the National Key Research and Development Program of China (Grant No. 2018YFB0704300). The first author thanks the China Scholarship Council (CSC) for financial support (202006460065).

References

1 R. Ferrando, J. Jellinek and R. L. Johnston, *Chem. Rev.*, 2008, **108**, 845–910.
2 F. Baletto and R. Ferrando, *Rev. Mod. Phys.*, 2005, **77**, 371.
3 I. Mosleh and A. Abbaspourrad, *RSC Adv.*, 2021, **11**, 32615–32621.
4 X. Cheng, X. Sui, J. Xu, X. Liu, M. Chen and Y. Zhu, *RSC Adv.*, 2021, **11**, 32526–32532.
5 L. Li, Y.-Z. Wang, X.-X. Wang, K.-K. Song, X.-D. Jian, P. Qian, Y. Bai and Y.-J. Su, *J. Phys. Chem. C*, 2020, **124**, 8706–8715.
6 X. Zhao, Y. Chang, J. Ji, J. Jia and M. Jia, *RSC Adv.*, 2021, **11**, 33179–33185.
7 Y. Tuo, Q. Lu, C. Chen, T. Liu, Y. Pan, Y. Zhou and J. Zhang, *RSC Adv.*, 2021, **11**, 26326–26335.
8 L. Li, H. Xin Ma, X. Dong Jian, P. Qian and Y. Jing Su, *Phys. Chem. Chem. Phys.*, 2020, **22**, 9467–9476.
9 D. Cheng, W. Wang, S. Huang and D. Cao, *J. Phys. Chem. C*, 2008, **112**, 4855–4860.
10 I. Parsina and F. Baletto, *J. Phys. Chem. C*, 2010, **114**, 1504–1511.
11 H. Zhang, L. Lu, K. Kawashima, M. Okumura, M. Haruta and N. Toshima, *Adv. Mater.*, 2015, **27**, 1383–1388.
12 H. Zhang, T. Watanabe, M. Okumura, M. Haruta and N. Toshima, *Nat. Mater.*, 2011, **11**, 49–52.
13 M. K. Samantaray, V. D'Elia, *et al.*, *Chem. Rev.*, 2020, **120**, 734–813.
14 L. Liu and A. Corma, *Chem. Rev.*, 2018, **118**, 4981–5079.
15 Y. Ren, X. Liu, Z. Zhang and X. Shen, *Phys. Chem. Chem. Phys.*, 2021, **23**, 15564–15573.
16 J. S. Jirkovsky, I. Panas, E. Ahlberg, M. Halasa, S. Romani and D. J. Schiffrin, *J. Am. Chem. Soc.*, 2011, **133**, 19432–19441.
17 J. Mao, J. Yin, J. Pei, D. Wang and Y. Li, *Nano Today*, 2020, **34**, 100917.
18 K. R. Reddy, K. P. Lee, A. I. Gopalan, M. S. Kim, A. M. Showkat and Y. C. Nho, *J. Polym. Sci., Part A: Polym. Chem.*, 2006, **44**, 3355–3364.
19 J. Chen, G. Xia, P. Jiang, Y. Yang, R. Li, R. Shi, J. Su and Q. Chen, *ACS Appl. Mater. Interfaces*, 2016, **8**, 13378–13383.
20 S. Shen, T. Zhao, J. Xu and Y. Li, *J. Power Sources*, 2010, **195**, 1001–1006.
21 G. Hu, F. Nitze, E. Gracia-Espino, J. Ma, H. R. Barzegar, T. Sharifi, X. Jia, A. Shchukarev, L. Lu, C. Ma, G. Yang and T. Wågberg, *Nat. Commun.*, 2014, **5**, 5253.
22 X. Zhang, D. Wu and D. Cheng, *Electrochim. Acta*, 2017, **246**, 572–579.
23 Z.-P. Wu, S. Shan, Z.-H. Xie, N. Kang, K. Park, E. Hopkins, S. Yan, A. Sharma, J. Luo and J. Wang, *ACS Catal.*, 2018, **8**, 11302–11313.
24 J. Wu, S. Shan, J. Luo, P. Joseph, V. Petkov and C.-J. Zhong, *ACS Appl. Mater. Interfaces*, 2015, **7**, 25906–25913.
25 W. Tang, L. Zhang and G. Henkelman, *J. Phys. Chem. Lett.*, 2011, **2**, 1328–1331.
26 L. Zhang, F. Hou and Y. Tan, *Chem. Commun.*, 2012, **48**, 7152–7154.
27 L.-B. Shi, Y.-Y. Zhang, X.-M. Xiu and H.-K. Dong, *Carbon*, 2018, **134**, 103–111.
28 L.-B. Shi, M. Yang, S. Cao, Q. You, Y.-Y. Niu and Y.-Z. Wang, *Appl. Surf. Sci.*, 2019, **492**, 435–448.
29 X. Wang, C. Wang, S. Ci, Y. Ma, T. Liu, L. Gao, P. Qian, C. Ji and Y. Su, *J. Mater. Chem. A*, 2020, **8**, 23488–23497.
30 Q. Liu, H. Zhao, X. Wang, J. Huo, L. Li, P. Gao, P. Qian, Y. Su and N. Chen, *Prog. Nat. Sci.: Mater. Int.*, 2019, **29**, 525–532.
31 K. H. Pham and T. T. T. Giap, *RSC Adv.*, 2021, **11**, 32435–32445.
32 G. Kresse and J. Furthmüller, *Comput. Mater. Sci.*, 1996, **6**, 15–50.
33 J. P. Perdew, K. Burke and M. Ernzerhof, *Phys. Rev. Lett.*, 1996, **77**, 3865–3868.
34 P. E. Blöchl, *Phys. Rev. B: Condens. Matter Mater. Phys.*, 1994, **50**, 17953–17979.
35 A. A. Peterson, F. Abild-Pedersen, F. Studt, J. Rossmeisl and J. K. Nørskov, *Energy Environ. Sci.*, 2010, **3**, 1311–1315.
36 J. K. Nørskov, J. Rossmeisl, A. Logadottir, L. Lindqvist, J. R. Kitchin, T. Bligaard and H. Jónsson, *J. Phys. Chem. B*, 2004, **108**, 17886–17892.
37 S. Plimpton, *J. Comput. Phys.*, 1995, **117**, 1–19.
38 X. Zhou, R. Johnson and H. Wadley, *Phys. Rev. B: Condens. Matter Mater. Phys.*, 2004, **69**, 144113.
39 X. W. Zhou, H. N. G. Wadley, R. A. Johnson, D. J. Larson, N. Tabat, A. Cerezo, A. K. Petford-Long, G. D. W. Smith, P. H. Clifton, R. L. Martens and T. F. Kelly, *Acta Mater.*, 2001, **49**, 4005–4015.
40 Q. Li, M. Wang, Y. Liang, L. Lin, T. Fu, P. Wei and T. Peng, *Phys. E: Low-Dimens. Syst. Nanostructures*, 2017, **90**, 137–142.
41 D. Schebarchov, S. Hendy and W. Polak, *J. Phys.: Condens. Matter*, 2009, **21**, 144204.
42 B. K. Teo and N. J. A. Sloane, *Inorg. Chem.*, 1985, **24**, 4545–4558.
43 I. A. Solov'yov, A. V. Solov'yov, W. Greiner, A. Koshelev and A. Shutovich, *Phys. Rev. Lett.*, 2003, **90**, 053401.
44 E. Pahl, F. Calvo, L. Koči and P. Schwerdtfeger, *Angew. Chem., Int. Ed.*, 2008, **47**, 8207–8210.
45 A. P. Tsai, *Sci. Technol. Adv. Mater.*, 2008, **9**, 013008.
46 Y. Shichibu, K. Suzuki and K. Konishi, *Nanoscale*, 2012, **4**, 4125–4129.
47 J. K. Seo, A. Khetan, M. H. Seo, H. Kim and B. Han, *J. Power Sources*, 2013, **238**, 137–143.

48 J. K. Nørskov, T. Bligaard, A. Logadottir, J. Kitchin, J. G. Chen, S. Pandelov and U. Stimming, *J. Electrochem. Soc.*, 2005, **152**, J23.
49 B. Hinnemann, P. G. Moses, J. Bonde, K. P. Jørgensen, J. H. Nielsen, S. Horch, I. Chorkendorff and J. K. Nørskov, *J. Am. Chem. Soc.*, 2005, **127**, 5308–5309.
50 T. Yang, Y. Bao, W. Xiao, J. Zhou, J. Ding, Y. P. Feng, K. P. Loh, M. Yang and S. J. Wang, *ACS Appl. Mater. Interfaces*, 2018, **10**, 22042–22049.
51 J. H. Ryu, S. S. Han, D. H. Kim, G. Henkelman and H. M. Lee, *ACS Nano*, 2011, **5**, 8515–8522.
52 W. Tang, E. Sanville and G. Henkelman, *J. Phys.: Condens. Matter*, 2009, **21**, 084204.
53 M. C. S. Escaño, *Nano Res.*, 2015, **8**, 1689–1697.
54 H. Xu, D. Cheng and Y. Gao, *ACS Catal.*, 2017, **7**, 2164–2170.
55 M. T. Darby and M. Stamatakis, *ChemPhysChem*, 2021, **22**, 499.
56 A. S. Nair and B. Pathak, *J. Phys. Chem. C*, 2019, **123**, 3634–3644.
57 J. Shin, J.-H. Choi, P.-R. Cha, S. K. Kim, *et al.*, *Nanoscale*, 2015, **7**, 15830–15839.
58 A. S. Nair and B. Pathak, *J. Phys. Chem. C*, 2019, **123**, 3634–3644.
59 D.-H. Lim and J. Wilcox, *J. Phys. Chem. C*, 2012, **116**, 3653–3660.
60 Y. Wang, H. Yuan, Y. Li and Z. Chen, *Nanoscale*, 2015, **7**, 11633.
61 L. Wang, L. Huang, F. Liang, S. Liu, Y. Wang and H. Zhang, *Chin. J. Catal.*, 2017, **38**, 1528–1539.
62 R. Subbaraman and S. K. Sankaranarayanan, *Phys. Rev. B: Condens. Matter Mater. Phys.*, 2011, **84**, 075434.
63 Q. Liu, Y. Su, K. Song, X. Wang, P. Gao, C. Wang, Y. Xiao, X. Jian and P. Qian, *Prog. Nat. Sci.: Mater. Int.*, 2020, **30**, 477–484.
64 P. Pawlow, *Z. fur Phys. Chem*, 1909, **65**, 1–35.